1-1-2018

Vacancy-induced sodium-ion storage in N-doped carbon Nanofiber@MoS2nanosheet arrays

Jiaojiao Liang
Hunan University

Zengxi Wei
Hunan University

Caiyun Wang
University of Wollongong, caiyun@uow.edu.au

Jianmin Ma
Hunan University, Xian University of Technology

Vacancy-induced sodium-ion storage in N-doped carbon Nanofiber@MoS2nanosheet arrays

Abstract

As a promising material for sodium-ion batteries, molybdenum disulphide (MoS2) affords excellent electrochemical performance owing to its large surface area and the accelerated electron transport within individual layers. However, it suffers from slow reaction kinetics and agglomeration owing to low conductivity and high surface energy. In this work, nitrogen-doped carbon nanofiber@MoS2nanosheets arrays with S-vacancies (NC@MoS2-VS) are developed via a process involving electrospining, hydrothermal and annealing. When served as an anode material for SIBs, this material displays a superior capacity of 495 mAh g−1over 100 charge/discharge cycles at a current density of 100 mA g−1, and the pseudocapacitive contribution is up to 74.4% as revealed by the cyclic voltammogram (CV) at 1 mV s−1. The theoretical calculations show that the presence of sulfur vacancies facilitates the adsorption of Na+and enhances the conductivity of MoS2. This work may pave a new avenue to develop other types of metal sulfides for high-performance SIBs.

Disciplines

Engineering | Physical Sciences and Mathematics

Publication Details

Liang, J., Wei, Z., Wang, C. & Ma, J. (2018). Vacancy-induced sodium-ion storage in N-doped carbon Nanofiber@MoS2nanosheet arrays. Electrochimica Acta, 285 301-308.

Vacancy-Induced Sodium-ion Storage in Cable Structure: N-doped Carbon@MoS_2 Nanosheets

Jiaojiao Liang,[a,|] Zengxi Wei,[a,|] Quanhui Liu,[a] Caiyun Wang[b] and Jianmin Ma[a,c,*]

[a]*School of Physics and Electronics, Hunan University, Changsha, 410082, P. R. China*

[b]*ARC Centre of Excellence for Electromaterials Science, Intelligent Polymer Research Institute, University of Wollongong, New South Wales 2522, Australia*

[c]*Key Laboratory of Adv.Energy Mater. Chemistry (Ministry of Education), Nankai University, Tianjin 300071,P.R. China*

| J.J. Liang and Z.X. Wei are equally contributed to this work.

Corresponding author: Jianmin Ma

Email: nanoelechem@hnu.edu.cn

Abstract As a promising electrode candidate for sodium-ion batteries, layered molybdenum disulphide (MoS_2) may afford excellent electrochemical performance owing to its large surface area and the accelerated electron transport within individual layer. However, it suffers from slow reaction kinetics and material agglomeration owing to low conductivity and high surface energy. In this work, a cable structure, nitrogen-doped carbon nanofiber@MoS_2 nanosheets with S-vacancies (NC@MoS_2-VS) is developed via a straightforward electrospining-hydrothermal and annealing process. When served as an anode material for SIBs, this material displays a superior capacity of 495 mAh g^{-1} over 100 charge/discharge cycles at a current density of 100 mA g^{-1} and the pseudocapacitive contribution is up to 74.4% in the 1mV s^{-1} with cyclic voltammetry (CV). And the theoretical calculations show that the presence of sulfur vacancies facilitates the adsorption of Na^+ and enhances the conductivity of MoS_2. This work may pave a new avenue to develop other type metal sulfides for high-performance SIBs.

Keywords: S-vacancies; MoS_2; Nanosheets; Cable structure; Sodium-ion batteries

1. Introduction

In recent years, sodium-ion batteries (SIBs) have attracted widespread attention due to the low cost and abundance of sodium, and better safety. [1-3] However, the heavier mass of sodium ion has larger radius (0.102 nm) than lithium (0.069 nm), which results in the slow de-intercalation of Na^+ in the electrode material, affecting the cycling and rate performance of SIBs.[4, 5] Meanwhile, the standard electrode potential (-2.71V vs. SHE) of Na^+/Na is much higher than that of Li^+/Li (-3.04V vs. SHE), leading to the lower energy density of SIBs than that of lithium-ion batteries (LIBs). [6] Therefore, it is challenging explore high-energy-density electrode materials with the large reversible intercalation of sodium ions.

As a typical two-dimensional (2D) layered material, molybdenum sulfide (MoS_2) has been considered as a promising electrode candidate for SIBs due to its structural characteristics, the large intrinsic interlayer spacing (0.62 nm) benefiting the intercalation of Na ions and affording the high theoretical specific capacity of 670 mAh g^{-1} .[7, 8] However, MoS_2 usually displays slow reaction dynamics during charge/discharge processes due to its high surface energy and low electronic conductivity.[9, 10] Furthermore, its layered structure is easily aggregated, leading to reduced active sites for Na^+ interaction.[11, 12] The volume change of MoS_2 in the charge/discharge processes can also result in severe pulverization of the electrode deteriorating the performance.[13, 14] In order to overcome these problems, electronically conductive carbon matrices are proposed to enhance the electrochemical performance of MoS_2, such as MoS_2/graphene composites, MoS_2/CNT composites, MoS_2/C nanofibers and MoS_2/carbon spheres.[15-18] Moreover, some research groups have studied the sulfur vacancy of MoS_2 materials to improve its electrochemical activity and adsorption energy to enhance its catalytic performance for hydrogen evolution reaction and electrochemical activity for Li_2S deposition.[19, 20]

In this work, we design a cable structure of nitrogen-doped carbon nanofiber@MoS_2 nanosheets by electrospining and hydrothermal methods, followed by introducing sulphur vacancies (S vacancies) through using of H_2 reduction annealing under Ar/H_2 atmosphere (denoted as: NC@MoS_2-VS). Theoretical calculations show that the S vacancies are new active sites which make the adsorption Na^+ strongly and the conductivity of MoS_2 enhanced, which well agrees with the experimental results. When used as anode material for the SIBs, the NC@MoS_2-VS displayed a discharging capacity of 495 mAh g^{-1} at the current density of 100mAg^{-1} for 100 cycles and the pseudocapacitive contribution of 74.4% at the scan rate of 1 mVs^{-1}. The strategy is promisingly applied in other metal sulfides as high-performance materials for SIBs.

2. Experimental Section

2.1 Synthesis

All the reagents were used as received without any treatment. Nitrogen-doped carbon nanofibers and MoS_2 nanosheets were synthesized according to the previous reports.[21, 22] Briefly, nitrogen-doped carbon nanofibers were prepared by electrospinning a solution containing 0.6 g of polyacrylonitrile (PAN, MW=150000, Sigma-Aldrich Co., Ltd) in 7 g of N,N-dimethylformamide (DMF, Sinopharm Chemical Reagent Co., Ltd.) at a flow rate of about 0.6 ml/h. The distance between the aluminum collector and needle was around 12 cm, and the voltage applied was 8 kV. The collected materials were pre-oxidized at 230 ℃ in air for 2h, followed by a carbonization process at 600 °C for 2h in Ar to form nitrogen-doped carbon nanofibers. The nitrogen-doped carbon nanofiber@MoS_2 nanoflower (NC@MoS_2) were synthesized via a hydrothermal reaction as follows: 12 mmol thiourea was added into a solution (15 ml ultrapure water and 15ml ethanol) containing 2 mmol $NaMoO_4$ under stirring for 30 min, followed by the addition of 80 mg carbon nanofibers; and the formed mixture solution was treated with ultrasonication for half an hour and then at 200 °C for 24 h in an oven. The NC@MoS_2 samples were collected and ultrasonic cleaned, drying in an oven at 60 °C for a night. The NC@MoS_2-VS samples were obtained by annealing precursor materials at 350 °C for 2h in Ar/H_2 atmosphere. As comparison, the NC@MoS_2 samples were treated at 350 °C for 2h in Ar gas and denoted as NC@MoS_2-Ar.

2.2 Characterization

The morphology and composition of the samples were characterized using scanning electron microscope (SEM, Hitachi S4800), high-resolution transmission electron microscope (TEM, Titan G2 60-300 with image corrector, America, at voltage of 300 kV), and X-ray diffractometer (Bruker D8 Adv). The samples were analyzed and determined by X-ray photoelectron spectroscopy (XPS, Thermo Scientific Escalab 250Xi), Raman scattering (LabRAM HR Evolution, HORIBA system, at an excitation wavelength of 532 nm) and a thermo-gravimetric analysis (a WCT-1D instrument, BOIF).

2.3 Electrochemical measurements

The CR2025-type half-cells were assembled in an argon-filled glove box ($O_2 \leq 0.5$ ppm, $H_2O \leq 0.5$ ppm). The working electrodes slurries were made by mixing the active materials (NC@MoS_2-VS, NC@MoS_2-Ar and NC@MoS_2; 80 %) with sodium carboxymethyl cellulose (CMC; 10 %) binder and acetylene black (10 %) in deionized water and ethanol, which was coated onto a Cu foil current collector and dried in a vacuum oven at 60 °C for 24 h. The working electrode and sodium foil (counter electrode and reference electrode) was separated by glass

microfiber filter membrane (Whatman, grade GF/A) saturated with electrolyte. The electrolyte was 1 M of $NaClO_4$ in a mixture of an EC and diethyl carbonate (DEC) solution at a volume ratio of 1:1 with 5 % fluoroethylene carbonate (FEC). The electrochemical performance measurements were carried out by Neware Battery Testing system, and the test voltage was between 0.001 and 3.0 V versus Na^+/Na. The electrochemical impedance spectroscopy (EIS) over a frequency range from 100 kHz to 0.01Hz and the cyclic voltammetry measurement were performed with the CHI 660e Electrochemical Workstation.

2.4 Methodology for DFT Calculations

The DFT calculations were carried out by using the Vienna Ab-initio Simulation Package (VASP)，[23, 24] with an exchange-correlation functional as described by the Perdew-Burke-Ernzerhof generalized gradient approximation (PBE-GGA) method,[25] and interaction between core electrons and valence electrons, using the frozen-core projector-augmented wave (PAW) method[26, 27]. Wave functions were expanded in a plane wave basis with a high energy cut-off of 400 eV and 3×3×1 for the numbers of k-point that can ensure the convergence for the total energy. The convergence criterion was set to 10^{-5} eV between two ionic steps for the self-consistency process, and 0.02eV/Å was adopted for the total energy calculations. To avoid interactions between adjacent images, a vacuum region of 15 Å was added along the normal direction to the monolayer. The adsorption energy (E_{ad}) of the Na atom at the sites in MoS_2 and MoS_2-VS (MoS_2 with sulphur vacancies) was calculated as follows:

$$E_{ad} = E_{MoS_2,MoS_2\text{-}VS+Na} - (E_{MoS_2,MoS_2\text{-}VS} + E_{Na})$$

Where E_{ad}, $E_{MoS_2,MoS_2\text{-}VS+Na}$, $E_{MoS_2,MoS_2\text{-}VS}$ and E_{Na} are the total energies for the different adsorption sites with one Na atom in MoS_2 and MoS_2-VS, for MoS_2 and MoS_2-VS without the adsorption of Na, and for one Na atom in the same slab, respectively.

The interaction between the MoS_2 or MoS_2-VS and Na ion implies a substantial charge transfer. This can be visualized by three-dimensional charge difference which can be defined as follow:

$$\Delta\rho = \rho_{MoS_2(MoS_2\text{-}VS)/Na} - \rho_{MoS_2(MoS_2\text{-}VS)} - \rho_{Na}$$

Where $\rho_{MoS_2(MoS_2\text{-}VS)/Na}$ ， $\rho_{MoS_2(MoS_2\text{-}VS)}$ **Error! Reference source not found.** and **Error! Reference source not found.** are the charge densities of the composite, respectively.

3. Results and discussion

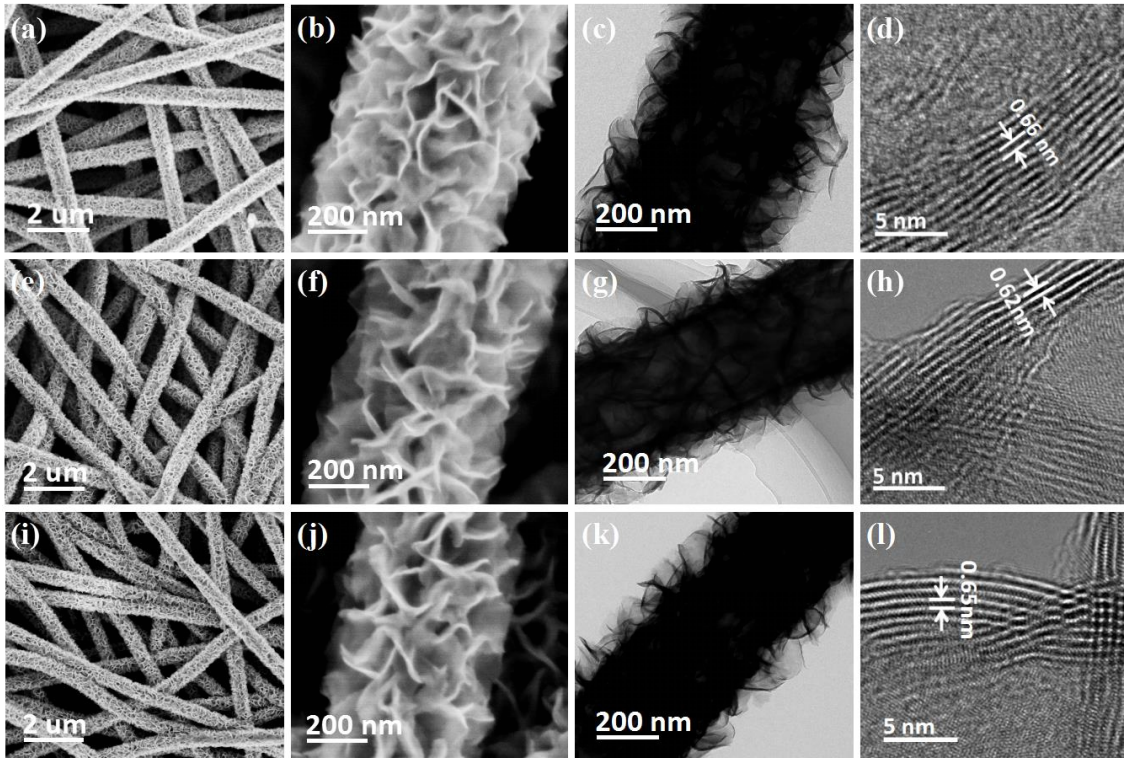

Figure 1. SEM images (a, b) and TEM images (c, d) of NC@MoS_2;SEM images (e, f) and TEM images (g, h) of NC@MoS2-Ar; SEM images (i, j) and TEM images (k, l) of NC@MoS_2-VS.

The morphology and crystal structure of NC@MoS_2, NC@MoS_2-Ar and NC@MoS_2-VS are characterized by SEM and TEM as shown in Figure 1. From the low-magnification SEM image of three materials (**Figure 1 a, e** and **i** correspond to NC@MoS_2, NC@MoS_2-Ar and NC@MoS_2-VS respectively), the MoS_2 nanosheets uniformly grown on the surface of each nitrogen-doped carbon nanofiber, and these nanosheets were vertically erected with carbon nanofibers as skeleton support creating a 3D porous structure from the high-magnification SEM image (**Figure 1b, f** and **j**). This unique cable structure could prevent the agglomeration of MoS_2 nanosheets and provide more active sites for the storage of sodium ions.[28, 29] The NC@MoS_2, NC@MoS_2-Ar and NC@MoS_2-VS displayed much similar morphology and structure, suggesting that the annealing temperature and annealing atmospheres did not have special effect on the surface except the diameter of material slightly slender due to the adsorbed of water and the sulfur evaporate during the high temperature and H_2 atmosphere, which can also be verified by the similar low-magnification TEM image as displayed in **Figure 1c, g** and **k**. In addition, from the high-magnification TEM images, one can find that the crystal lattice distance of 0.66 nm for NC@MoS_2 and 0.62 nm for NC@MoS_2-Ar are corresponded to the lattice plane (002) as revealed by the high-magnification TEM

images (**Figure 1d** and **h**), probably because of the better crystallinity of MoS_2 during the annealing process. And the broadening lattice of 0.65 nm for NC@MoS_2-VS (**Figure 1l**) could be related with the formation of defect annealing in Ar/H_2 and contributing to the transmission of Na^+.[8, 30]

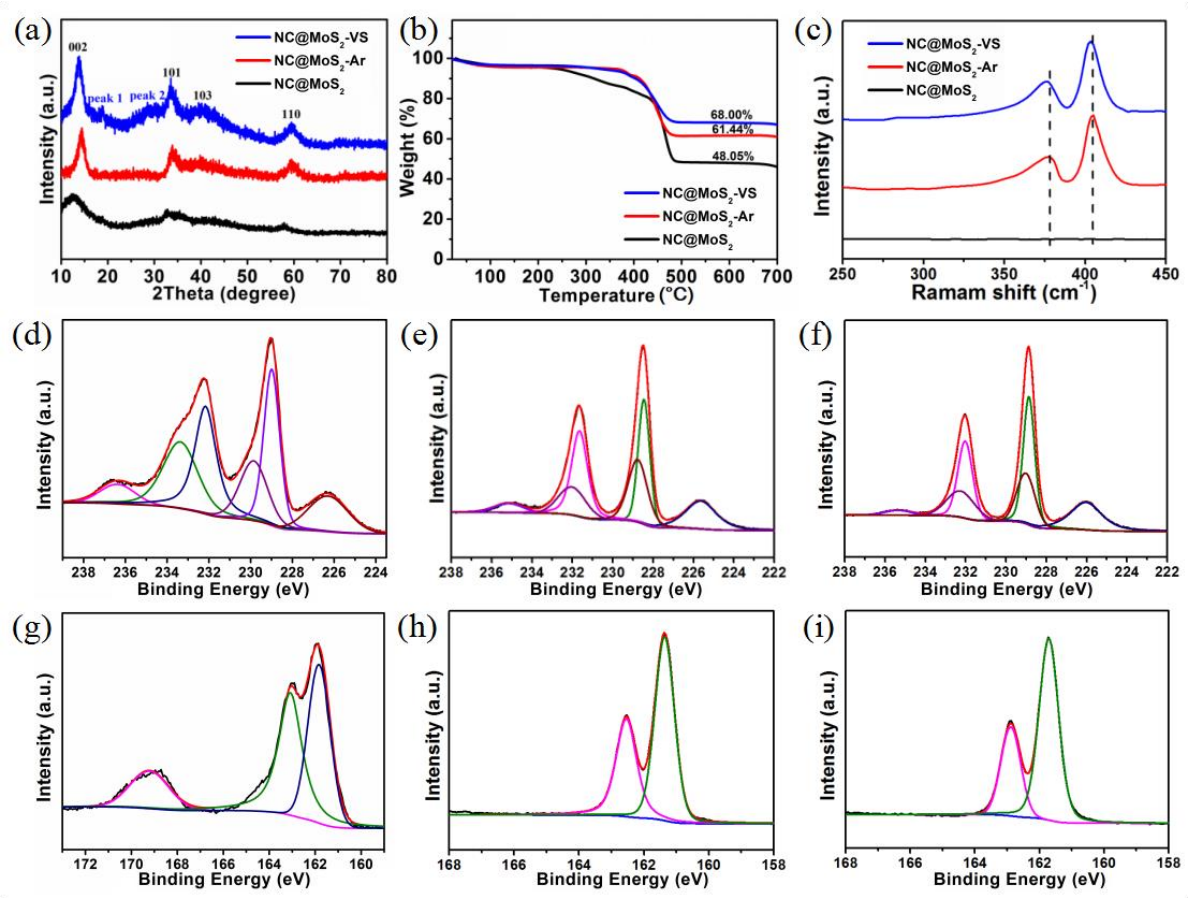

Figure 2. (a) XRD patterns, (b) TGA and (c) Raman spectrum of NC@MoS_2-VS, NC@MoS_2-Ar and NC@MoS_2; XPS spectra of (Mo 3d, S 2p) for (d, g) NC@MoS_2, (e, h) NC@MoS_2-Ar and (f, i) NC@MoS_2-VS.

The XRD patterns of NC@MoS_2, NC@MoS_2-Ar and NC@MoS_2-VS demonstrated the dominant peaks at 14.40, 33.45, 39.50 and 58.23º as displayed in the **Figure 2a**, corresponding to the lattice planes (002), (101), (103) and (110) of hexagonal 2H-MoS_2 (PDF standard card 24-513). And these peaks of NC@MoS_2 are broad indicating a low degree of crystallinity before annealing. Additionally, the appearance of two new peaks and the negative shift of (002) peak for NC@MoS_2-VS may be related to the T-MoS_2 generated during the annealing process,[31, 32] which is consistent with the broaden of lattice plane (002) in the TEM images. Moreover, the content of MoS_2 is were analyzed in air from 30 to 700 °C by the TGA curve for the NC@MoS_2, NC@MoS_2-Ar and NC@MoS_2-VS (**Figure 2b**) thought calculated with the weight of MoO_3 (48.05%, 61.44% and 68.00%), which is oxidized by

MoS_2, corresponding to about 54.06%, 69.12% and 76.50%, respectively. The weight loss of NC@MoS_2 is attributed to the evaporation of adsorbed water and the decomposition of excessive sulfate ion from 250 to 400 ℃, and the weight retention of NC@MoS_2-VS is little more than that of NC@MoS_2-Ar due to the asportation of some sulfur by Ar/H_2 annealing. The Raman peaks of NC@MoS_2-VS, NC@MoS_2-Ar and NC@MoS_2 are shown in **Figure 2c**. And the NC@MoS_2 did not present any peaks at the wavelength from 250 to 450 cm^{-1} in the Raman spectrum, which might be due to the poor crystallinity of MoS_2. After an annealing treatment in Ar, the formed NC@MoS_2-Ar displayed two main peaks at 378 cm^{-1} and 405 cm^{-1} corresponding to the in-plane E^1_{2g} and out-of-plane A_{1g} vibration modes of MoS_2. These two modes were also detected at 376 cm^{-1} and 404 cm^{-1} for NC@MoS_2-VS, which is annealed in Ar/H_2. The slight shift of these two peaks may be ascribed to sulfur vacancies. It is reported that the existence of some sulfur vacancies can result in the difference in frequency and the E^2_{1g} and A_{1g} peaks broadening.[33, 34]

The surface valence state and chemical component of these materials at different annealing atmospheres were investigated using XPS. And the NC@MoS_2-VS presented the peaks of elements Mo, S, N, O and C (**Figure S1**). The high resolution spectra of Mo 3d and S 2p for NC@MoS_2, NC@MoS_2-Ar and NC@MoS_2-VS are recorded as displayed in **Figure 2d-i**. The binding energies of Mo 3d and S 2p of NC@MoS_2 are displayed in Fig. 2d and g, Mo 3d can be divided into these binding energies, of which 236.4 eV corresponds to Mo^{6+} of MoO_3, and 233.4, 232.2, 229.9, 229.0 eV correspond to Mo^{4+} 3d in 2H-MoS_2, and 226.3 eV corresponds to S 2s peak of MoS_2.[35] S 2p can be divided into 169.2eV and 163.1, 161.8eV and corresponded to S^{4+} species in sulfate groups, S $2p_{1/2}$ and $2p_{3/2}$, respectively.[36] In addition, the Mo 3d and S 2p of NC@MoS_2-Ar are shown in Fig. 2e and h. The binding energies of Mo 3d could be divided into 235.2eV, 232.0 and 229.0eV, 231.7 and 228.8 eV, and 225.6 eV, corresponding to the Mo 3d of MoO_3, 2H-MoS_2, 1T-MoS_2 and S 2s of MoS_2, respectively. The binding energies of 162.5 and 161.4 eV of NC@MoS_2-Ar are discovered, which match with the S 2p1/2 and 2p3/2, respectively. And the binding energies of Mo 3d for NC@MoS_2-VS could be divided into 232.3 eV of 3d3/2 and 229.0 eV of 3d5/2, and center in 1T-MoS_2 observes at 231.0 eV of 3d3/2 and 228.8 eV of 3d5/2,[37-39] other two peaks at 235.4 and 226.0 eV correlating to Mo^{6+} 3d5/2 of MoO_3 and S 2s of MoS_2.[40] The peaks of S 2p can be resolved into two peaks of 162.9and 161.7 eV, corresponding to S 2p1/2 and 2p3/2, respectively.[41] The peaks of C 1s and N 1s are resolved into the binding energies as displayed in **Figure S2**. The peaks of 286.6, 285.01 and 284.2 eV are accorded to the binding energies of C-O-C, C-H and C-C, respectively.[42-44] Two binding energies of 395.3 and 394.7eV are related to the Mo3p and the peak located at 398.2 eV corresponds to pyridinic-N,[45, 46] evidencing

the presence of nitrogen in NC@MoS_2-VS. The peaks of Mo^{6+} 3d and S for NC@MoS_2-VS can be offset to a higher binding energy of 0.2-0.4eV than that of the NC@MoS_2-Ar, which indicates that NC@MoS_2-VS possess higher oxidation state of Mo after an annealing process in Ar/H_2, suggesting the lack of sulfur.[47] In addition, the atomic percentages of Mo, S, O and C for NC@MoS_2, NC@MoS_2-Ar and NC@MoS_2-VS are shown in Table S1, and the atomic ratio of S to Mo 3d in NC@MoS_2-VS is 1.47, much lower than that about 2.23 for NC@MoS_2-Ar and NC@MoS_2, proving the lack of sulfur.[20] All these results manifest that the sulfur vacancies do exist in NC@MoS_2-VS.

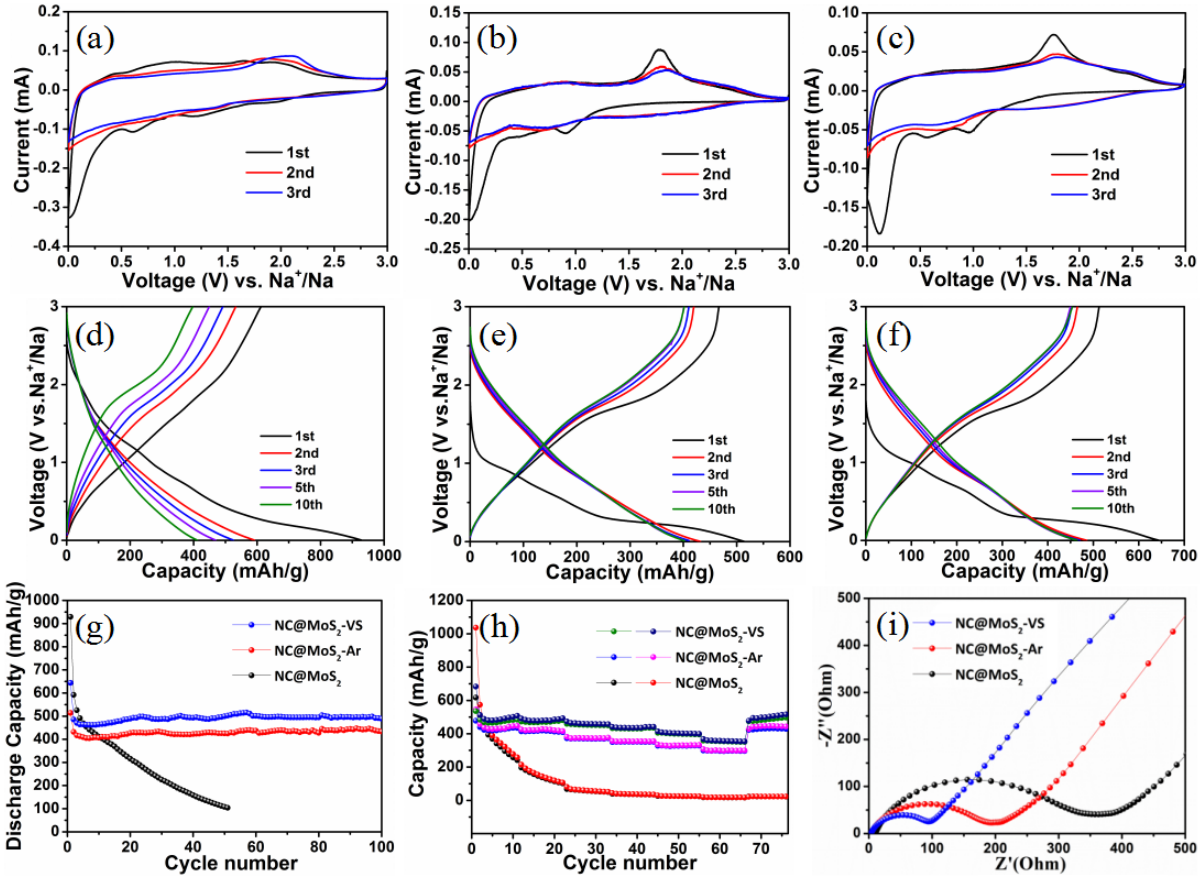

Figure 3. Cyclic voltammetry curves of (a) NC@MoS_2, (b) NC@MoS_2-Ar, (c) NC@MoS_2-VS; Charge-discharge curves of (d) NC@MoS_2, (e) NC@MoS_2-Ar, (f) NC@MoS_2-VS; (g) Cycling performances of NC@MoS_2, NC@MoS_2-Ar and NC@MoS_2-VS; (h) Rate capabilities of NC@MoS_2, NC@MoS_2-Ar and NC@MoS_2-VS and (i) Nyquist plots of NC@MoS_2, NC@MoS_2-Ar and NC@MoS_2-VS.

The electrochemical performances of NC@MoS_2, NC@MoS_2-Ar and NC@MoS_2-VS as anode materials of SIBs are displayed in **Figure 3**. The CV curves of the NC@MoS_2, NC@MoS_2-Ar and NC@MoS_2-VS electrodes were performed between 0.001 V to 3.0 V vs. Na^+/Na at a scan rate of 0.1 $mV \cdot s^{-1}$ and shown in **Figure 3a-c**. These

three curves have a very close trend, only the redox peak of NC@MoS_2 is not obvious, probably because the crystal of MoS_2 form is not well with unannealed. In the first cycle, it displayed three reduction peaks at potentials of 0.8-1.1 V, 0.5-0.8 V and 0-0.3 V. They can be ascribed to the formation of a solid-electrolyte interface (SEI) layer, conversion of MoS_2 into Na_xMoS_2 owing to the continuous insertion of Na^+,[48] and conversion reaction from Na_xMoS_2 to Mo under 0.3 V,[49] respectively. The broad potentials of the oxidization peak appeared at 1.5-2.1 V, corresponding to vulcanizing Mo particles to MoS_2.[49] In the 2nd and 3rd curves, the reduction peaks at 0.5-1.0 V and oxidation peaks situate at 1.5-2.1 V were nearly overlapped. The charge-discharge curves of NC@MoS_2, NC@MoS_2-Ar and NC@MoS_2-VS are displayed in **Figure 3d-f**, the charge/discharge capacity of NC@MoS_2 and NC@MoS_2-Ar are 612/929 $mAhg^{-1}$ and 432/514 $mAhg^{-1}$ at the first cycle, corresponding to the Coulomb efficiency of 65.9% and 63.7%, respectively. And the first charge/discharge capacity and the Coulombic Efficiency of NC@MoS_2-VS are 486/644 $mAhg^{-1}$ and 75.5%. And the first Coulombic Efficiency of NC@MoS_2-VS is upper to these of NC@MoS_2 and NC@MoS_2-Ar, indicating the better of storage sodium for NC@MoS2-VS. The cycling performances of these electrodes at a current density of 100mAg^{-1} are demonstrated in the **Figure 3g**. The NC@MoS_2-VS shows a higher specific capacity of 495 mAh g^{-1} for 100 cycles, compared with that 430$mAhg^{-1}$ and 103 mAh g^{-1} for NC@MoS_2-Ar and NC@MoS_2. In addition, the NC@MoS_2-VS electrode presents the better rate capacities (**Figure 3h**). It delivered a capacity of 510, 485, 460, 438, 400 and 355 mAh g^{-1} at the current density of 50, 100, 300, 500, 1000 and 2000 mA g^{-1}, respectively, much higher than that 446, 425, 375, 350, 330 and 299 $mAhg^{-1}$ afforded by the NC@MoS_2-Ar electrodes. A nearly capacity of 500 mAh g^{-1} could be restored after the current density recovered to 100 mA g^{-1}, and the NC@MoS_2 electrodes exhibited the worst rate capacities. The comparison of rate properties with other MoS_2@C composite is shown **Figure S3** and the NC@MoS_2-VS material exhibited excellent rate performance. The electrochemical impedance spectroscopy (EIS) analysis of the NC@MoS_2-VS, NC@MoS_2-Ar and NC@MoS_2 were carried out, and the Nyquist plots are showed in **Figure 3i**. It is clearly found that the semicircular diameter of NC@MoS_2-VS is smaller than that of the NC@MoS2-Ar and NC@MoS_2 in the high frequency region, indicating that the NC@MoS_2-VS has high conductivity because of the existence of sulfur vacancies.[50, 51] In the low frequency region, the straight slope of NC@MoS_2-VS and NC@MoS_2-Ar are close, and both are higher than that of the NC@MoS_2. It indicates that the annealing could improve the conductivity of materials and contribute them to the transport of sodium ions.[4] The improved Na storage performance of NC@MoS_2-VS could be attributed to the unique heterogeneous structure, widen lattice of MoS_2 and the presence of sulfur vacancies. Firstly, the heterogeneous structure composed of MoS_2 nanosheets

vertically grown on the N-doped carbon nanofibers could provide a conductive network to guide the transmission of electronic, and accommodate the agglomeration of nanosheets during de-intercalation Na^+ processes. Secondly, the widen lattice of the MoS_2 in NC@MoS_2 could accelerate the transfer of Na ions. Thirdly, the annealing of NC@MoS_2-VS in Ar/H_2 reducing atmosphere induces the formation of S-vacancies, which facilitates the adsorption of sodium ions and increases the conductivity of MoS_2.

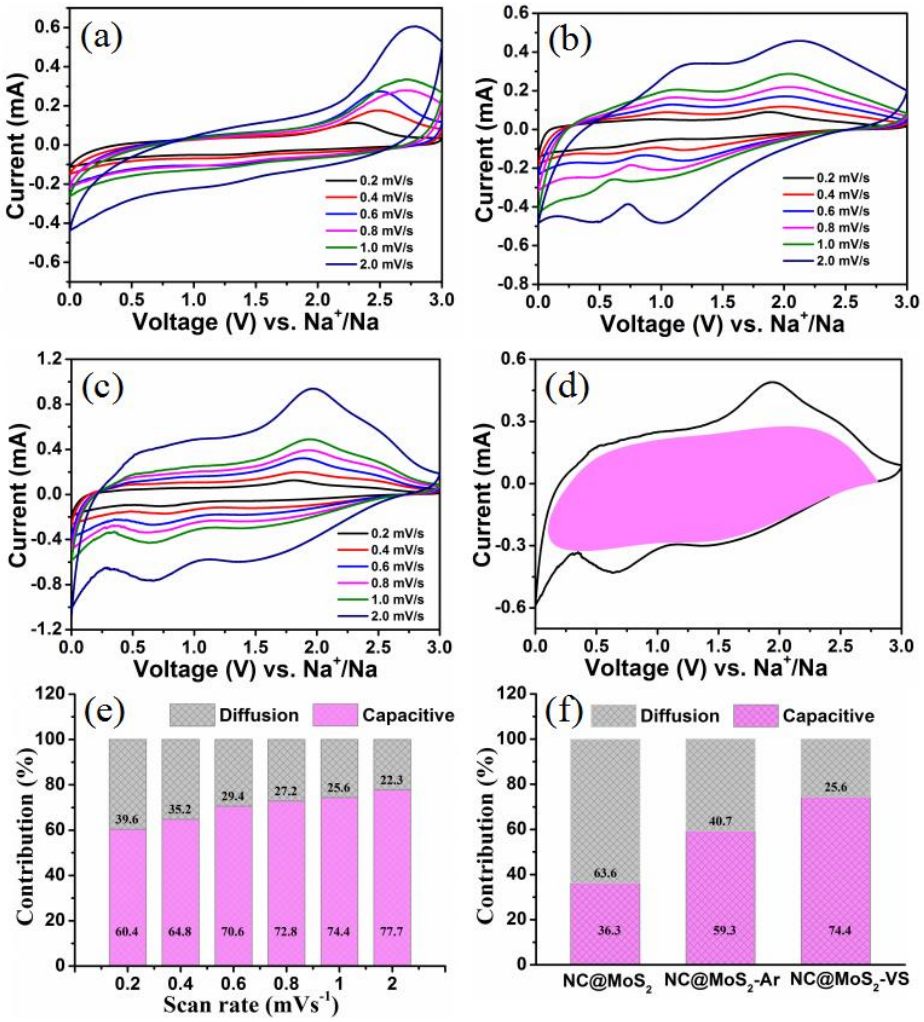

Figure 4. Cyclic voltammetry curves of (a) NC@MoS_2, (b) NC@MoS_2-Ar, (c) NC@MoS_2-VS from 0.2 to 2 mVs^{-1}; (d) Capacitive contributions (pink regions) at 1.0 mVs^{-1} for NC@MoS_2-VS; The contribution ratio of capacitive and diffusion (e) at different scan rates for NC@MoS_2-VS and (f) at 1.0 mVs^{-1} for diverse materials.

To explore further the sodium storage in NC@MoS_2, NC@MoS_2-Ar and NC@MoS_2-VS by utilizing the different scan rate CV curves, the capacitive effect and the diffusion-controlled Na^+ intercalation effects to the total sodium storage according to the reference article and they can be expressed by the equation:[52, 53] $i(V)=k_1v+k_2v^{1/2}$, $i(V)$ corresponds to the current value at the voltages, v refers to the scan rate, k_1v refers to the

contribution of the capacitive effect provided by the surface-adsorbing charge and $k_2v^{1/2}$ refers to the solid diffusion control with intercalated/de-intercalated charges. The CV curves at scan rates from 0.2 to 2 mVs^{-1} of NC@MoS_2, NC@MoS_2-Ar and NC@MoS_2-VS are shown in the Figure **4(a-c)**, and the kinetic analysis of NC@MoS_2 and NC@MoS_2-Ar are demonstrated in the **Figure S4** and **S5**. The slope of $i(V)/v^{1/2}$ vs. $v^{1/2}$ for NC@MoS_2-VS at various potentials in discharge and charge process as displayed in the **Figure S6**. **Figure 4d** shows the pink regions of capacitive current contributions with NC@MoS_2-VS are matched according to different voltage corresponding to different current values at a scan rate of 1 mVs^{-1}, and the contribution ratio of capacitive effect and diffusion-controlled in order are 62.3%, 64.8%, 70.6%, 72.8%, 74.4%, 77.7% and 37.7%, 35.2%, 29.4%, 27.2%, 25.6%, 22.3% from 0.2 mV s^{-1} to 2 mV s^{-1} as shown in the **Figure 4e**. **Figure 4f** shows the contribution ratio of capacitive effect for NC@MoS_2, NC@MoS_2-Ar and NC@MoS_2-VS corresponding to 36.3%, 53.9%, 74.4% at 1 mV s^{-1}, and the ratios of contribution for capacitance effect during Na^+ storage at different scan rates are displayed in **Table S2**. They indicate that the capacitive effect of NC@MoS_2-VS play a major role in sodium storage performance.

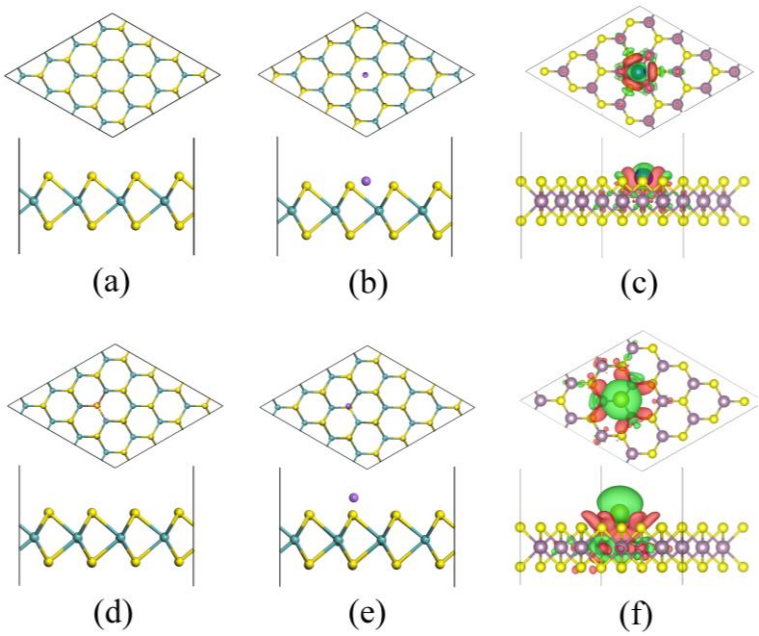

Figure 5. (a) and (b) Atomic structure of pure monolayer MoS_2 supercell in the simulation and adsorption site of a Na atom; (c) Three-dimensional difference charge density for the pure monolayer MoS_2 supercell in the simulation and adsorption site of a Na atom with an isovalue of 0.003 e/$Å^3$. (d) and (e) The favorite structure of S-vacancies decorated monolayer MoS_2 and the possible adsorption position of Na atom, respectively. (f) Three-dimensional difference charge density for the MoS_2-VS with an adsorption site of a Na atom with an isovalue of 0.003 e/$Å^3$. The dash line ring represented the vacancies of Sulphur atom. Red and green isosurfaces

represent charge accumulation and depletion in the space with respect to isolated MoS_2 (MoS_2-VS) and Na.

To gain an in-depth understanding of the enhanced Na^+ storage behavior in NC@MoS_2-VS, the density functional theory (DFT) was performed to illuminate the difference of Na^+ adsorption behavior on the pure MoS_2 surface and MoS_2 surface decorated by S-vacancies. **Figure 5a, b, d and e** show the typical models of a Na atom at the sites in MoS_2 and MoS_2-VS (S-vacancies map with red dash line ring), respectively. Our theoretical results indicate that the S-vacancies modified MoS_2 surface not only significantly increase the electronic conductivity of MoS_2, but also effectively improve the storage/diffusion capability of Na^+.[54, 55] The adsorption behavior of Na on both pure MoS_2 and MoS_2-VS are also calculated, and the results are summarized **Table S1**. The adsorption energy of the Na in MoS_2-VS is -2.302 eV, which is much small than that in pure MoS_2 (-0.248 eV), which indicates that MoS_2-VS of NC@MoS_2-VS is more feasible for Na storage and diffusion than pure MoS_2. The interaction between Na ion and the slab suggests a substantial charge transfer (MoS_2 and MoS_2-VS) from the Na ion to MoS_2 or MoS_2-VS. The three-dimensional charge density difference could prove the different interaction for pure MoS_2 or MoS_2-VS with a Na atom. **Figure 5c** shows the three-dimensional charge density difference in the MoS_2/Na composite, where the electron-rich and hole-rich regions are distributing obviously. The charge accumulation appears on the S atoms, which are below the Na atom. On the contrary, the charge depletion is found on the Na ion. We can find that the charge localize substantially on the vacancy of S atom of MoS_2-VS (**Figure 5f**) than that of pure MoS_2. Meanwhile, the charge depletion of Na atom is relatively large than that of Na atom in pure MoS_2, which is indicated that the interaction between Na atom and MoS_2-VS is larger than that of Na atom in the pure MoS_2. In addition, the bader charge analysis shows that 0.842 e of the Na atom is adsorbed onto the MoS_2-VS surface, as show in **Table S3**. Only 0.525 e, however, of the Na atom transfer to pure MoS_2 surface (**Table S3**), which indicates a weak interaction between pure MoS_2 and Na atom. Summarily, it is concluded that the presence of S-vacancies MoS_2 increases the adsorption energy of Na atoms, and more Na atoms can be trapped on the MoS_2-VS surface.

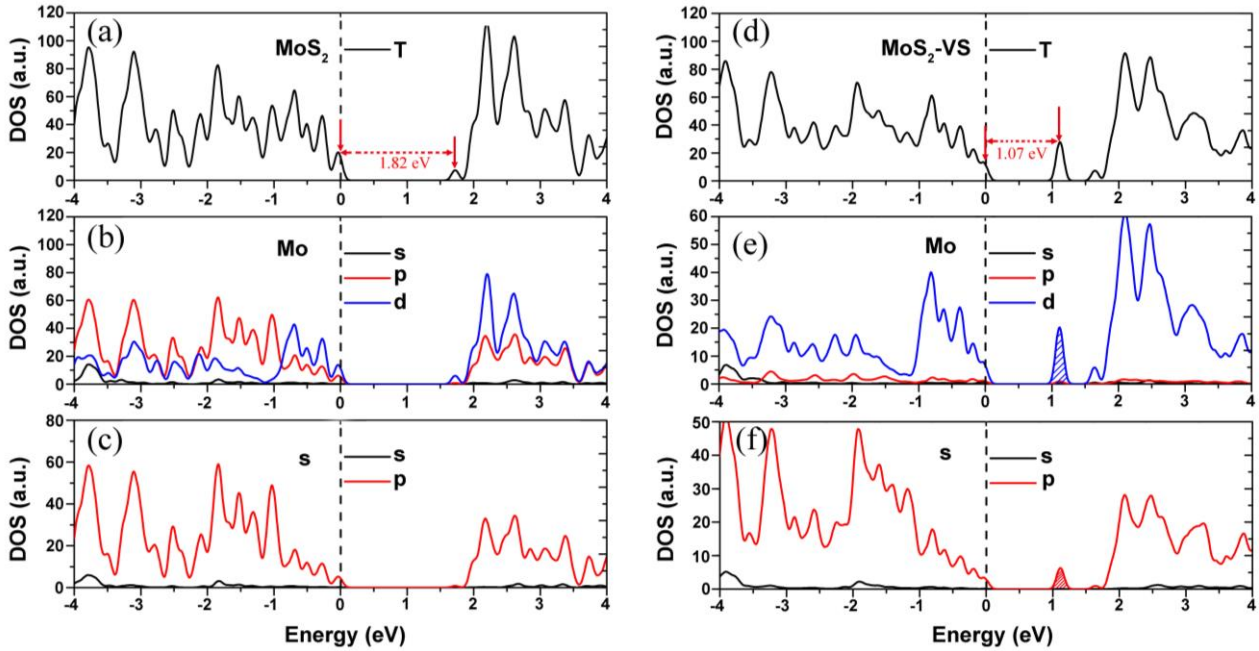

Figure 6. (a-c) The DOSs of pure MoS_2 and PDOSs of Mo and S, respectively; (d-f) The DOSs of S-vacancies decorated MoS_2 and PDOSs of Mo and S of MoS_2-VS. The Fermi level is set to zero.

Based on the typical structure models, the partial density of states (PDOSs) of pure MoS_2 and MoS_2-VS have been performed, as shown in **Figure 6**. Compared to pure MoS_2, the MoS_2-VS has a smaller band gap (1.07 *vs.* 1.82 eV, **Figure 6a** and **d**), owing to the formation of defect level in the conduction band (CB) of the electronic structure. We also find that the defect level is dominant by the Mo 4d and S p orbit (**Figure 6e** and **f**), which moves toward low energy from high energy in the CB of pure MoS_2 (**Figure 6b** and **c**). The lower CB minimum (CBM) could enhance the transfer of electron and hole pairs, thereby leading to an enhanced electronic conductivity of MoS_2-VS. These results indicate that the S-vacancies decorated MoS_2 have a bright ability to boost the conductivity in monolayer MoS_2.

4. Conclusions

In conclusion, the NC@MoS_2-VS has been successfully synthesized, with introducing the S-vacancies by Ar/H_2 annealing and broadening the lattice of MoS_2. Meanwhile, the result of theoretical calculation confirmed that the S-vacancies can enhance the adsorption energy of sodium ions and improve the conductivity of the material. Moreover, the result of experimental data indicated that the storage sodium performance of NC@MoS_2-VS is better than the NC@MoS_2-Ar and NC@MoS_2. The NC@MoS_2-VS exhibited a discharge capacity of 495 mAh g^{-1} for 100 cycles, and the pseudocapacitive contribution is as high as 74.4% at the 1mV/s. Moreover, the presence of sulfur

vacancies for MoS_2 material has enhanced adsorption capacity of Na^+ and improved its conductivity by the theoretical calculations. The excellent Na storage performance of NC@MoS_2-VS could be attributed to unique heterogeneous structure, introducing sulfur vacancies of NC@MoS_2-Ar and widen lattice of MoS_2.

Acknowledgments

This work was supported by the National Natural Science Foundation of China (Grant No. 51302079), and the National Natural Science Foundation of Hunan Province (Grant No. 2017JJ1008).

References

[1] X. Duan, J. Xu, Z. Wei, J. Ma, S. Guo, H. Liu, S. Dou, Atomically thin transition-metal dichalcogenides for electrocatalysis and energy storage, Small Methods, 1 (2017), 1700156.
[2] L. Wang, Y.-G. Sun, L.-L. Hu, J.-Y. Piao, J. Guo, A. Manthiram, J. Ma, A.-M. Cao, Copper-substituted $Na_{0.67}Ni_{0.3-x}Cu_x$ $Mn_{0.7}O_2$ cathode materials for sodium-ion batteries with suppressed P_2-O_2 phase transition, J. Mater. Chem. A, 5 (2017) 8752-8761.
[3] J. Xu, Y. Dou, Z. Wei, J. Ma, Y. Deng, Y. Li, H. Liu, S. Dou, Recent progress in graphite intercalation compounds for rechargeable metal (Li, Na, K, Al)-ion batteries, Adv. Sci., 4 (2017) 1700146.
[4] Y. Cai, H. Yang, J. Zhou, Z. Luo, G. Fang, S. Liu, A. Pan, S. Liang, Nitrogen doped hollow MoS_2/C nanospheres as anode for long-life sodium-ion batteries, Chem. Eng. J., 327 (2017) 522-529.
[5] M. Mao, C. Cui, M. Wu, M. Zhang, T. Gao, X. Fan, J. Chen, T. Wang, J. Ma, C. Wang, Flexible ReS_2 nanosheets/N-doped carbon nanofibers-based paper as a universal anode for Alkali (Li, Na, K) ion battery, Nano Energy, 45(2018) 346-352.
[6] X. Xu, Z. Fan, X. Yu, S. Ding, D. Yu, X.W. Lou, A nanosheets-on-channel architecture constructed from MoS_2 and CMK-3 for high-capacity and Long-cycle-life lithium storage, Adv. Energy Mater., 4 (2015) 1400902.
[7] C. Cui, Z. Wei, J. Xu, Y. Zhang, S. Liu, H. Liu, M. Mao, S. Wang, J. Ma, S. Dou, Three-dimensional carbon frameworks enabling MoS_2 as anode for dual ion batteries with superior sodium storage properties, Energy Storage Mater., 15 (2018) 22-30.
[8] C. Zhao, C. Yu, M. Zhang, Q. Sun, S. Li, M.N. Banis, X. Han, Q. Dong, J. Yang, G. Wang, Enhanced sodium storage capability enabled by super wide-interlayer-spacing MoS_2 integrated on carbon fibers, Nano Energy, 41 (2017) 66-74.
[9] B. Wang, Y. Zhang, J. Zhang, R. Xia, Y. Chu, J. Zhou, X. Yang, J. Huang, Facile synthesis of a MoS_2 and functionalized graphene heterostructure for enhanced lithium-storage performance, ACS Appl. Mater. Interfaces, 9 (2017) 12907-12913.
[10] C. Zhang, Z. Wang, Z. Guo, X.W. Lou, Synthesis of MoS_2-C one-dimensional nanostructures with improved lithium storage properties, ACS Appl. Mater. Interfaces, 4 (2012) 3765-3768.
[11] Y. Yuan, F. Huang, A. Pan, W. Xiao, Enhanced lithium storage properties of hierarchical MoS_2-rGO nanosheets, Int. J. Electrochem. Sci, 12 (2017) 5431-5437.
[12] W. Sun, P. Li, X. Liu, J. Shi, H. Sun, Z. Tao, F. Li, J. Chen, Size-controlled MoS_2 nanodots supported on reduced graphene oxide for hydrogen evolution reaction and sodium-ion batteries, Nano Res., 10 (2017) 2210-2222.

[13] J. Zhou, J. Qin, X. Zhang, C. Shi, E. Liu, J. Li, N. Zhao, C. He, 2D space-confined synthesis of few-layer MoS_2 anchored on carbon nanosheet for lithium-ion battery anode, ACS nano, 9 (2015) 3837-3848.
[14] Y.M. Chen, X.Y. Yu, Z. Li, U. Paik, X.W. Lou, Hierarchical MoS_2 tubular structures internally wired by carbon nanotubes as a highly stable anode material for lithium-ion batteries, Sci Adv, 2 (2016) e1600021.
[15] L. David, R. Bhandavat, G. Singh, MoS_2/graphene composite paper for sodium-ion battery electrodes, ACS nano, 8 (2014) 1759-1770.
[16] X. Zhang, X. Li, J. Liang, Y. Zhu, Y. Qian, Synthesis of MoS_2@C nanotubes via the Kirkendall effect with enhanced electrochemical performance for lithium ion and sodium ion batteries, Small, 12 (2016) 2484-2491.
[17] X. Xiong, W. Luo, X. Hu, C. Chen, L. Qie, D. Hou, Y. Huang, Flexible membranes of MoS_2/C nanofibers by electrospinning as binder-free anodes for high-performance sodium-ion batteries, Sci. Rep., 5 (2015) 9254.
[18] Z. Wan, J. Shao, J. Yun, H. Zheng, T. Gao, M. Shen, Q. Qu, H. Zheng, Core-shell structure of hierarchical quasi-hollow MoS_2 microspheres encapsulated porous carbon as stable anode for Li-Ion batteries, Small, 10 (2014) 4975-4981.
[19] C. Tsai, H. Li, S. Park, J. Park, H.S. Han, J.K. Nørskov, X. Zheng, F. Abild-Pedersen, Electrochemical generation of sulfur vacancies in the basal plane of MoS_2 for hydrogen evolution, Nat. Commun., 8 (2017) 15113.
[20] H. Lin, L. Yang, X. Jiang, G. Li, T. Zhang, Q. Yao, G.W. Zheng, J.Y. Lee, Electrocatalysis of polysulfide conversion by sulfur-deficient MoS_2 nanoflakes for lithium–sulfur batteries, Energy Environ. Sci., 10 (2017) 1476-1486.
[21] J. Liang, C. Yuan, H. Li, K. Fan, Z. Wei, H. Sun, J. Ma, Growth of SnO_2 nanoflowers on N-doped carbon nanofibers as anode for Li- and Na-ion batteries, Nano-Micro Lett., 10 (2017) 21.
[22] T. Yang, Y. Chen, B. Qu, L. Mei, D. Lei, H. Zhang, Q. Li, T. Wang, Construction of 3D flower-like MoS_2 spheres with nanosheets as anode materials for high-performance lithium ion batteries, Electrochim. Acta, 115 (2014) 165-169.
[23] G. Kresse, J. Furthmuller, Efficiency of ab-initio total energy calculations for metals and semiconductors using a plane-wave basis set, Comput. Mater. Sci., 6 (1996) 15-50.
[24] G. Kresse, J. Hafner, Ab initio molecular dynamics for liquid metals, Phys. Rev. B: Condens. Matter, 47 (1993) 558-561.
[25] J.P. Perdew, K. Burke, M. Ernzerhof, Generalized gradient approximation made simple, Phys. Rev. Lett., 77 (1996) 3865-3868.
[26] P.E. Blochl, Projector augmented-wave method, Phys. Rev. B: Condens. Matter, 50 (1994) 17953-17979.
[27] G. Kresse, D. Joubert, From ultrasoft pseudopotentials to the projector augmented-wave method, Phys. Rev. B: Condens. Matter, 59 (1999) 1758-1775.
[28] X. Zheng, J. Xu, K. Yan, H. Wang, Z. Wang, S. Yang, Space-confined growth of MoS_2 nanosheets within graphite: the layered hybrid of MoS_2 and graphene as an active catalyst for hydrogen evolution reaction, Chem. Mater., 26 (2014) 2344-2353.
[29] Z. Hu, L. Wang, K. Zhang, J. Wang, F. Cheng, Z. Tao, J. Chen, MoS_2 nanoflowers with expanded interlayers as high-performance anodes for sodium-ion batteries, Angew. Chem., 126 (2014) 13008-13012.
[30] B. Yuan, L. Zeng, X. Sun, Y. Yu, Q. Wang, Enhanced sodium storage performance in flexible free-standing multichannel carbon nanofibers with enlarged interlayer spacing, Nano Res., 11 (2018) 2256–2264.
[31] M. Wu, J. Zhan, K. Wu, Z. Li, B. Geng, L. Wang, D. Pan, Metallic 1T MoS_2 nanosheet arrays vertically grown on activated carbon fiber cloth for enhanced Li-ion storage performance, J. Mater. Chem. A, 5 (2017) 14061-14069.
[32] Q. Liu, X. Li, Q. He, A. Khalil, D. Liu, T. Xiang, X. Wu, L. Song, Gram-scale aqueous synthesis of stable few-layered 1T-MoS_2: applications for visible-light-driven photocatalytic hydrogen evolution, Small, 11 (2015) 5556-5564.

[33] P. Cheng, K. Sun, Y.H. Hu, Mechanically-induced reverse phase transformation of MoS_2 from stable 2H to metastable 1T and its memristive behavior, RSC Adv., 6 (2016) 65691-65697.
[34] H. Li, C. Tsai, A.L. Koh, L. Cai, A.W. Contryman, A.H. Fragapane, J. Zhao, H.S. Han, H.C. Manoharan, F. Abild-Pedersen, Activating and optimizing MoS_2 basal planes for hydrogen evolution through the formation of strained sulphur vacancies, Nat. Mater., 15 (2015) 48–53 .
[35] R. Anbazhagan, Y.A. Su, H.C. Tsai, R.J. Jeng, MoS_2-Gd chelate magnetic nanomaterials with core shell structure used as contrast agents in in vivo magnetic resonance imaging, ACS Appl. Mater. Interfaces, 8 (2015) 1827.
[36] B. Xie, Y. Chen, M. Yu, T. Sun, L. Lu, T. Xie, Y. Zhang, Y. Wu, Hydrothermal synthesis of layered molybdenum sulfide/N-doped graphene hybrid with enhanced supercapacitor performance, Carbon, 99 (2016) 35-42.
[37] S. Bai, L. Wang, X. Chen, J. Du, Y. Xiong, Chemically exfoliated metallic MoS_2 nanosheets: A promising supporting co-catalyst for enhancing the photocatalytic performance of TiO_2 nanocrystals, Nano Res., 8 (2015) 175-183.
[38] A. Ambrosi, Z. Sofer, M. Pumera, 2H→1T phase transition and hydrogen evolution activity of MoS_2, $MoSe_2$, WS_2 and WSe_2 strongly depends on the MX_2 composition, Chem. Commun., 51 (2015) 8450-8453.
[39] X. Geng, Y. Jiao, Y. Han, A. Mukhopadhyay, L. Yang, H. Zhu, Freestanding metallic 1T MoS_2 with dual ion diffusion paths as high rate anode for sodium-ion batteries, Adv. Funct. Mater., 27 (2017) 1702998.
[40] S.K. Jha, R. Kumari, S. Choudhary, P. Guha, P. Satyam, B.S. Yadav, Z. Naqvi, S. Kushvaha, R. Ratnesh, M. Mehata, Facile synthesis of semiconducting ultrathin layer of molybdenum disulfide, J. Nanosci. Nanotechnol., 18 (2018) 614-622.
[41] Y. Ren, Q. Xu, C. Wang, X. Zheng, Y. Jia, Y. Qi, Y. Zhou, X. Yang, Z. Zhang, CO_2-assisted solution-phase selective assembly of 2D WS_2-$WO_3 \cdot H_2O$ and 1T-2H MoS_2 to desirable complex heterostructures, ChemNanoMat, 3 (2017). 632-638
[42] J. Zhang, D. Zeng, H. Wang, Z. Qin, A. Pang, C. Xie, Highly responsive chemical sensing on NO_2 at room temperature based on reduced porous graphene, Mater. Lett., 204 (2017) 27-30.
[43] J. Chen, W. Mei, C. Liu, C. Hu, Q. Huang, N. Chen, J. Chen, R. Zhang, W. Hou, Carbon-modified bismuth titanate with an enhanced photocatalytic activity under nature sunlight, Mater. Lett., 172 (2016) 184-187.
[44] L. Mei, M. Mao, S. Chou, H. Liu, S. Dou, D.H. Ng, J. Ma, Nitrogen-doped carbon nanofibers with effectively encapsulated GeO2 nanocrystals for highly reversible lithium storage, J. Mater. Chem. A, 3 (2015) 21699-21705.
[45] D. Geng, M. Li, X. Bo, L. Guo, Molybdenum nitride/nitrogen-doped multi-walled carbon nanotubes hybrid nanocomposites as novel electrochemical sensor for detection l-cysteine, Sens. Actuators, B, 237 (2016) 581-590.
[46] J. Qiu, Z. Yang, Q. Li, Y. Li, X. Wu, C. Qi, Q. Qiao, Formation of N-doped molybdenum carbide confined in hierarchical and hollow carbon nitride microspheres with enhanced sodium storage properties, J. Mater. Chem. A, 4 (2016) 13296-13306.
[47] J. Jeon, J. Lee, G. Yoo, J.-H. Park, G.Y. Yeom, Y.H. Jang, S. Lee, Size-tunable synthesis of monolayer MoS_2 nanoparticles and their applications in non-volatile memory devices, Nanoscale, 8 (2016) 16995-17003.
[48] R. Wang, S. Gao, K. Wang, M. Zhou, S. Cheng, K. Jiang, MoS_2@rGO nanoflakes as high performance anode materials in sodium ion batteries, Sci. Rep., 7 (2017) 7963.
[49] X. Li, J. Li, Q. Gao, X. Yu, R. Hu, J. Liu, L. Yang, M. Zhu, MoS2 nanosheets with conformal carbon coating as stable anode materials for sodium-ion batteries, Electrochim. Acta, 254 (2017) 172-180.
[50] P. Zhang, F. Qin, L. Zou, M. Wang, K. Zhang, Y. Lai, J. Li, Few-layered MoS_2/C with expanding d-spacing as a high-performance anode for sodium-ion batteries, Nanoscale, 9 (2017) 12189-12195.
[51] F. Lu, M. Zhou, W. Li, Q. Weng, C. Li, Y. Xue, X. Jiang, X. Zeng, Y. Bando, D. Golberg, Engineering sulfur

vacancies and impurities in $NiCo_2S_4$ nanostructures toward optimal supercapacitive performance, Nano Energy, 26 (2016) 313-323.
[52] Z. Su, Z. Wei, C. Lai, H. Deng, Z. Liu, J. Ma, Robust pseudo-capacitive Li-I_2 battery enabled by catalytic, adsorptive N-doped graphene interlayer, Energy Storage Mater. 14 (2018) 129-135.
[53] X. Deng, Z. Wei, C. Cui, Q. Liu, C. Wang, J. Ma, Oxygen-deficient anatase TiO_2@C nanospindles with pseudocapacitive contribution for enhancing lithium storage, J. Mater. Chem. A, 6 (2018) 4013-4022.
[54] Z. Deng, H. Jiang, Y. Hu, Y. Liu, L. Zhang, H. Liu, C. Li, 3D Ordered macroporous MoS_2@C nanostructure for flexible Li-ion batteries, Adv. Mater., 29 (2017) 1603020.
[55] X. Xie, Z. Ao, D. Su, J. Zhang, G. Wang, MoS_2/graphene composite anodes with enhanced performance for sodium-ion batteries: the role of the two-dimensional heterointerface, Adv. Funct. Mater., 25 (2015) 1393-1403.